applied sciences

MDPI

Review

Methods of Atmospheric Coherence Length Measurement

Ming Li [1,2,*], Pengxin Zhang [1,2] and Jiawei Han [1,2]

[1] Tianjin Key Laboratory of Wireless Mobile Communications and Power Transmission, Tianjin Normal University, Tianjin 300387, China; zpx15294450825@163.com (P.Z.); hjwjohnny@126.com (J.H.)
[2] College of Electronic and Communication Engineering, Tianjin Normal University, Tianjin 300387, China
* Correspondence: mingli@tjnu.edu.cn

Abstract: Free-space optical (FSO) communication possesses the advantages of high security, large information capacity, high-speed transmission, small terminal size, low power consumption, easy and flexible deployment, etc. It is a promising communication technique, and could be an alternative to optical fiber communication and traditional radio frequency (RF) communication. One of principal challenges that FSO faces is the susceptibility of the atmospheric channel, which is turbulent in nature. After the optical signals propagate over the atmospheric channel, their wavefronts suffer from deleterious perturbation, thus resulting in degradation in the performance of the FSO. This knowledge with respect to FSO links helps to optimize the system design and reduce the adverse effects of atmospheric turbulence. The atmospheric coherence length of FSO links reflects the atmospheric turbulence effects, and it is one of the key parameters of FSO systems. Measuring the atmospheric coherence length, as a result, is of great interest as well as importance to the FSO community. In this paper, several methods associated with atmospheric coherence length measurement are reviewed.

Keywords: atmospheric coherence length; free space optical communication; atmospheric turbulence

Citation: Li, M.; Zhang, P.; Han, J. Methods of Atmospheric Coherence Length Measurement. *Appl. Sci.* **2022**, *12*, 2980. https://doi.org/10.3390/app12062980

Academic Editor: Periklis Petropoulos

Received: 20 January 2022
Accepted: 9 March 2022
Published: 15 March 2022

1. Introduction

Conventional radio frequency (RF) systems suffer from vulnerability to interference, bandwidth limitations, high power consumption and frequency licensing, while free-space optical (FSO) communications are not subject to these limitations. The laser beam has a highly narrow divergence, which enables immunity against eavesdropping. Even free-space quantum optical communication can provide unconditional information security [1,2]. Compared to radio spectrum resources, which are highly regulated, optical frequencies are not regulated and can be readily used. Additionally, the terminals in FSO are more compact and consume less energy than those in RF. Accordingly, the FSO system can be deployed in less time. The above advantages make FSO a promising communication technique [3–6]. However, the FSO links are easily affected by deleterious atmospheric turbulence effects [7–11]. Atmospheric turbulence is generated due to the continuous mixing of air temperatures and the formation of turbulent motion under the action of wind. Atmospheric turbulence is actually a process of continuous energy transfer. As the wind speed and its Reynolds number increases, locally unstable air masses are generated. This is known as an eddy. The largest eddy, with a size of L_0, is called the outer scale of turbulence (typically in dozens to hundreds of meters), while the smallest eddy, with a size of l_0, is referred to as the inner scale of turbulence (typically in a few millimeters). Under the influence of inertial forces, the large eddies split into smaller ones. The eddy that is smaller than the inner scale l_0 belongs to the viscous dissipation region, where the turbulent eddy is dissipated into heat. Eddies between l_0 and L_0 form the inertial subrange. The atmospheric turbulence, in turn, causes random perturbations to the atmospheric refractive index in the temporal and spatial domains [12–14].

After optical signals propagate through the free-space channel, both the wavefront phases and amplitudes will produce random fluctuations due to the presence of atmospheric turbulence. Therefore, the optical signals are distorted, which markedly degrades

the performance of FSO. In this regard, measuring the turbulence intensity and understanding the characteristics and transformation laws of turbulence are of great interest and importance to FSO. The atmospheric coherence length reflects the turbulence intensity and characterizes the magnitude of both the phase and amplitude fluctuations of the optical waves. Thus, the atmospheric coherent length measurement can be used for the evaluation of FSO links [4,7,8,11–13,15–17] as well as for other optical applications operating over atmosphere, such as optical imaging [18,19], optical remote sensing [20,21], etc.

The atmospheric coherence length is defined as the coherence distance of the phase in the beam cross section after the optical beam is transmitted over the atmospheric channel in the presence of turbulence. This concept was first introduced by Fried in his study of the structure function of the wavefront phase undulation [22]. The atmospheric coherent length is related to the integral over the propagation distance. Given that atmospheric turbulence is statistically homogeneous and isotropic, within the framework of the Kolmogorov model it can be expressed as $r_0 = \left(0.423k^2 \int_0^L C_n^2\,(z)dz\right)^{-\frac{3}{5}}$, where $k = 2\pi/\lambda$ is the wave number with λ being the optical signal wavelength; C_n^2 is the atmospheric refractive index structure parameter. This integral is applied along the entire path from the source to the destination L. When considering a horizontal FSO link, C_n^2 is often assumed to not vary and is a constant with $r_0 = \left(0.423C_n^2Lk^2\right)^{-\frac{3}{5}}$. The coherence length r_0 captures the total fluctuations induced by atmospheric turbulence. A smaller value of r_0 indicates a more severe disturbance of atmospheric turbulence [12]. Therefore, an essential part of studying the impact of atmospheric turbulence on FSO is the measurement of the atmospheric coherence length.

The currently existing methods for measuring the atmospheric coherence length can be divided into two categories: one is the retrieval of r_0 based on the atmospheric refractive index structure parameter C_n^2 , and the other is the coherence length r_0 direct measurement method. This paper presents a comprehensive review with respect to the atmospheric coherent length measurement methods. Sections 2 and 3 outline both measurement categories, respectively. A summary is presented in Section 4.

2. Retrieval of r_0 Based on C_n^2

The atmospheric coherence length r_0 can be easily derived from its definition, which is closely related to the value of C_n^2. If known C_n^2, one can calculate the value of r_0 by dint of the definition. This method is referred to as the retrieval of r_0 based on the atmospheric refractive index structure parameter, C_n^2. There are multiple methods to measure C_n^2, including the temperature structure measurement method, scintillation method and radar measurement method.

2.1. Temperature Structure Measurement Method

The principle of the temperature structure measurement method for measuring the atmospheric coherence length is that the transformation of temperature is measured using a temperature pulsation meter, and then the relationship between the temperature structure function and the atmospheric refractive index structure function is applied to find C_n^2 [12]. According to the Kolmogorov theory of atmospheric turbulence, the structure function of the temperature fluctuations is subject to the two-thirds universal law in the inertial range under the assumption of statistical homogeneity and isotropy

$$\begin{aligned} D_T(|r_1 - r_2|) &= \langle\, [T(r_1) - T(r_2)]^2 \,\rangle, \\ D_T(|r_1 - r_2|) &= C_T^2 |r_1 - r_2|^{2/3}, l_0 << R << L_0, \end{aligned} \tag{1}$$

where $T(r_1)$ and $T(r_2)$ denote the temperatures of two spatial points with r_1 and r_2 away from the reference point, respectively; C_T^2 is the temperature structure parameter; and $\langle \cdot \rangle$ indicates the ensemble average. Accordingly, C_T^2 can be expressed by

$$C_T^2 = \frac{\left\langle |T(r_1) - T(r_2)|^2 \right\rangle}{|r_1 - r_2|^{2/3}}. \tag{2}$$

Further, the atmospheric refractive index structure parameter C_n^2 is related to C_T^2 as

$$C_n^2 = (79 \times 10^{-6} \frac{P}{T^2})^2 C_T^2, \tag{3}$$

where P is the atmospheric pressure in millibar; and T is the atmospheric ambient temperature in K. Therefore, C_n^2 can be calculated by substituting Equation (2) into Equation (3). A schematic sketch of the traditional temperature structure measurement method is shown in Figure 1. The experimental setup contains four resistors, two standard resistors R and two platinum wire resistors, Rs_1 and Rs_2, which together form the Wheatstone bridge. The two standard resistors are allocated under the two platinum wire resistors Rs_1 and Rs_2, and Rs_1 and Rs_2 are located on the probes of a platinum wire thermometer separated by the length of r. The platinum wire thermometer measures the values of Rs_1 and Rs_2, which are eventually converted into $T(r_1)$ and $T(r_2)$. C_T^2 can be calculated by merely employing Equation (2). The temperature structure measurement method is able to provide the turbulence profile along the vertical direction, so it can also be adopted to reveal the relevant physical processes involved in the evolution of atmospheric turbulence. In practice, the sensor in Figure 1 is oriented following the streamwise.

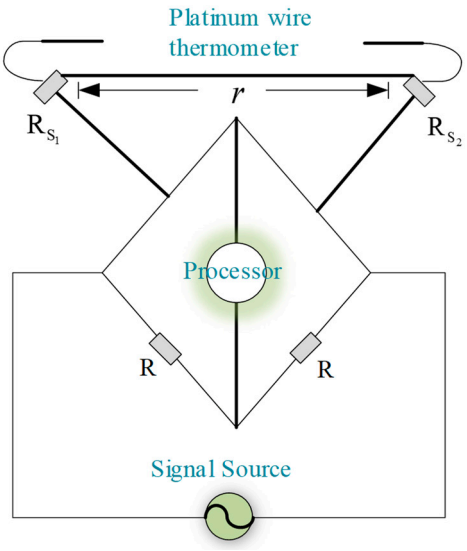

Figure 1. Schematic sketch of the temperature structure measurement method.

2.2. Scintillation Method

Due to the presence of atmospheric turbulence in the FSO link, the optical signal will experience arrival angle fluctuation at the receiving site. The temporal statistics related to the arrival angle fluctuation are known as the scintillation effect. It has been concluded that the scintillation is closely related to the atmospheric refractive index structure parameter C_n^2. Within the framework of the Kolmogorov model, C_n^2 can be expressed by [23,24]

$$C_n^2 = E\sigma_\chi^2 D_t^{7/3} L^{-3}, \tag{4}$$

where $E = 4.48D_r/D_t$ with D_r and D_t representing the diameter of the receiving aperture and the diameter of transmitting aperture, respectively; L is the propagation distance from source to destination; σ_χ^2 indicates the log-amplitude variance of the receiving optical field. Generally, the scintillation index denoted by β_I^2, which characterizes the light intensity scintillation intensity, is readily adopted instead of the log-amplitude variance. Under weak turbulence conditions ($\beta_I^2 < 1$), the scintillation index can be expressed by the log-amplitude variance σ_χ^2. It follows that [12]

$$\beta_I^2 = \exp(4\sigma_\chi^2) - 1. \tag{5}$$

In practice, the scintillation index is measured by

$$\beta_I^2 = \frac{\langle I^2 \rangle - \langle I \rangle^2}{\langle I \rangle^2}, \tag{6}$$

where I indicates the intensity of optical signal. By measuring β_I^2, C_n^2 can be calculated based on Equations (4)–(6). As such, the laser scintillation method measures the path-integrated atmospheric refractive index structure parameter C_n^2, and then performs the retrieval of the atmospheric coherence length r_0.

The scintillometer is a widely-used instrument to measure the scintillation index of optical signals traveling along a specific atmosphere path [12,23–28]. It is also commonly used as the ground-based equipment to evaluate new measurement approaches associated with C_n^2 [25]. Up to now, multiple scintillometers with diverse configurations have been proposed, including the large area scintillometer with two separate LED discs [25], the saturation-resistant scintillometer with large incoherent transmitting and receiving optics [23], the inner-scale-measurement scintillometer with two sets of transceivers [27], etc. Some of them are already commercially available [29], but all scintillometers are designed by following the principle mentioned above. A schematic sketch of a traditional scintillometer is shown in Figure 2. The instrument adopts a layout that consists of a transmitter, receiver, and data processing module. The specific workflow of the traditional scintillometer is as follows. The optical beam is emitted by the transmitter. After the beam propagates over the turbulent atmosphere in the middle, it reaches the receiver on the right side and is converted to an electrical signal. Eventually the data-processing module carries out an analysis of the demodulated electrical signals, and provides an evaluation of the scintillation index. In concrete terms, the produced electrical signal U is proportional to the emitted optical signal intensity I, thus Equation (5) becomes

$$\beta_I^2 = \frac{\langle I^2 \rangle - \langle I \rangle^2}{\langle I \rangle^2} = \frac{\langle U^2 \rangle - \langle U \rangle^2}{\langle U \rangle^2}. \tag{7}$$

Additionally, a deep machine learning algorithm has been presented to evaluate β_I^2 [30]. With the scintillation index β_I^2, one can calculate C_n^2 by merely substituting Equation (6) into Equation (4). Now based on C_n^2, the retrieval of the atmospheric coherence length r_0 is performed. We should note that scintillometers are susceptible to the scintillation saturation effect [26,31]. Therefore, the scintillometer would fail once it enters regions of strong turbulence ($\beta_I^2 \geq 1$) since scintillation saturation occurs. Fortunately, new techniques have sprung up to address such issues [23,32,33].

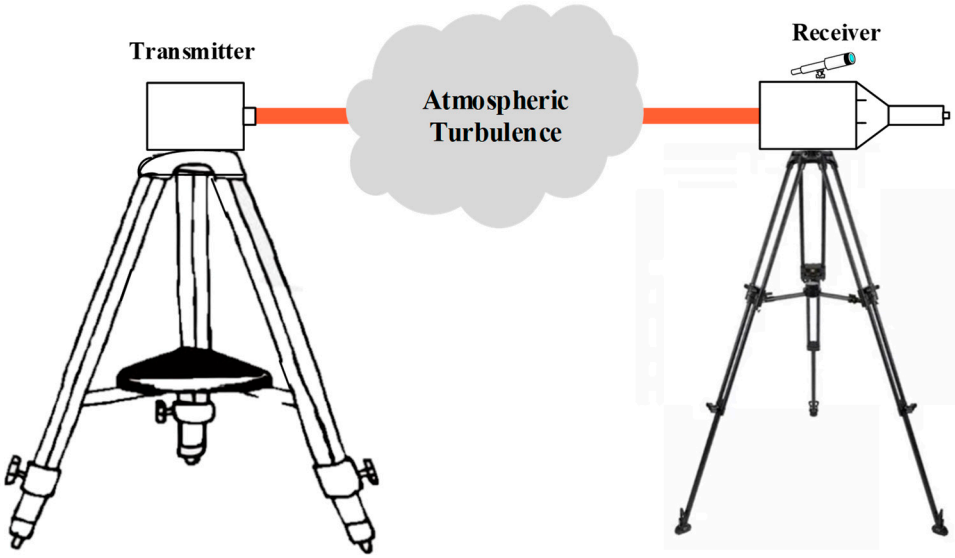

Figure 2. Schematic sketch of the traditional scintillometer.

2.3. Radar Measurement Method

As far as the radar measurement method is concerned, there are two strategies. One involves the backscattering cross section, while the other focuses on the emitted power. For the former, the radar signal carrier can be either acoustic or electromagnetic waves. Under the assumptions of isotropy and statistical homogeneity, the backscattering cross section for the case of acoustic waves can be expressed as [34]:

$$\rho_s(\theta) = \frac{\pi}{2}k^4\cos^2\theta[\frac{\Phi_T[2k\sin(\theta/2)]}{T^2} + \cos^2(\theta/2)\frac{V[2k\sin(\theta/2)]}{\pi c_a[2k\sin(\theta/2)]^2}], \tag{8}$$

where θ is the scattering angle; k is the wave number; T is the atmospheric temperature, c_a is the acoustic velocity, $\Phi_T[]$ is the temperature spectral function; and $V[]$ is the velocity spectral function. The expression for the backscattering cross section for the case of the electromagnetic wave is given by

$$\rho_s(r') = \frac{\pi}{2}k^4\Phi_T[2k\sin(\theta/2)]\sin^2 i(r'), \tag{9}$$

where $i(r')$ is the angle between the electric field vector and the line from the scatterer to observation point, with r' denoting the vector from the transmitter towards the scatterer. The temperature structure constant C_T^2 can be derived in light of the backscattering cross section ρ_s above [35],

$$C_T^2 = \frac{\rho_s \times T^2}{4 \times 10^{-3} \times \lambda^{-1/3}}. \tag{10}$$

Similar to the preceding temperature structure measurement method, since C_T^2 can be known, so can C_n^2. As such, a retrieval of the atmospheric coherence length r_0 is performed.

The other method is to directly measure the atmospheric refractive index structure parameter C_n^2 by employing the wind profile radar to evaluate its echo power P_s [36–38]:

$$C_n^2 = \frac{P_s r^2}{7.3 \times 10^{-4} \times P_t G(c\tau/2)E^2\lambda^{5/3}}, \tag{11}$$

where G is the gain; r is the radar-scatterer distance; E is the antenna loss; c is the speed of light; τ is the signal pulse width; P_t indicates the transmitted power. For a specific wind profile radar, the parameters G, r, E, c, τ, P_t are given. The return signal power, P_s is estimated directly from the original signal-to-noise ratio of the return signal obtained from

the wind profile radar by probing the atmosphere. Once C_n^2 has been calculated, one could perform the retrieval of r_0.

3. Coherence Length r_0 Direct Measurement Method

Studies have demonstrated that the measurement of C_n^2 will deteriorate due to the path and accuracy of the measurement. The temperature structure measurement method can only be used on the pylons at low altitude; hence, measurements at relatively high altitude cannot be acquired. The scintillometer has a limited measurement range due to the scintillation saturation effect. As for the radar measurement method, it is appropriate for fixed-point targets only, and it involves cumbersome installation and huge cost. To circumvent those drawbacks, the direct measurement of the atmospheric coherence length r_0 has been proposed, which includes the differential image motion monitor (DIMM), wavefront structure function method, slope difference method and wavefront phase variance method, wherein the Shack–Hartman wavefront sensor (SHWS) is applied. Note that the DIMM may use the CCD instead of the SHWS [39,40]. The SHWS is generally considered as one of the crucial components in the adaptive optics system, as it enables accurate and rapid measurement of the wavefront shape and phase information. It includes an array of chromium-mask microlenses that image the beam onto a CCD, creating a point-array distribution of the wavefront information. The wavefront of the optical signal is usually fitted with the Zernike polynomial. The Zernike polynomial coefficients are calculated based on the positions of the dot array on the CCD, which is eventually employed for wavefront reconstruction. As such, the reconstructed wavefront provides the basis for the measurement of atmospheric coherence length.

3.1. DIMM

The DIMM obtains the atmospheric coherence length r_0 by measuring the variance of the differential arrival angle [15,41,42]. Since the variance originates from the arrival angles over the two subapertures of the SHWS, DIMM eliminates other optical distortions in the FSO link, such as jitter resulting from the optical terminal platform and inherent distortions of the optics.

A schematic sketch of the arrival angle deviation is shown in Figure 3. The spot centroid of $(x_\mathrm{r}, y_\mathrm{r})$ from the aberrant wavefront imaging at the receiving plane deviates from its centroid of $(x_\mathrm{o}, y_\mathrm{o})$ when there is no aberration, and the relationship between the arrival angle α and the spot centroid is

$$x_r = \alpha f_L, y_r = x_r \cot \alpha, \tag{12}$$

where f_L denotes the focal length of the imaging lens. The angle-of-arrival undulation variance is

$$\alpha^2 = 0.340 \left(\frac{\lambda}{D}\right)^2 \left(\frac{d}{r_0}\right)^{5/3}, \tag{13}$$

where D is the diameter of the subaperture of the telescope and d is the distance between the centers of the two subapertures. The atmospheric coherence length measurement found by using the DIMM is shown in Figure 4.

In Figure 4, two relatively independent telescope lenses are shown on the left. The upper beam is reflected by the plane mirror to the attenuator and then passes through the filter. The lower light travels through the diaphragm and light wedge, and then reaches the imaging mirror of the CCD together with the upper light. By doing so, the arrival angle deviation can be measured. After several observations, one can obtain the arrival angle undulation variance.

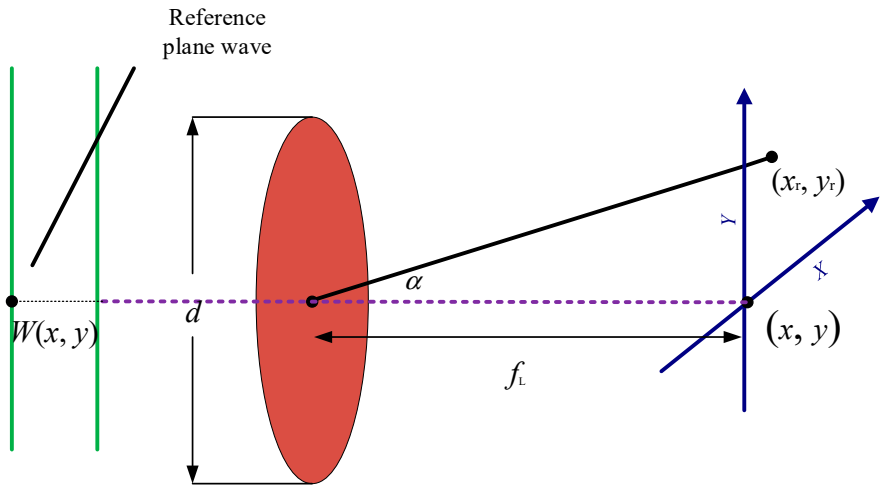

Figure 3. Schematic sketch of the wavefront deviation.

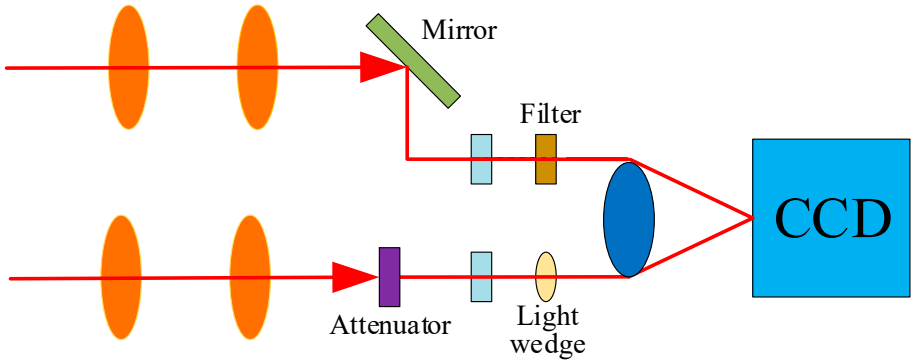

Figure 4. Sketch of the DIMM.

In 1990, Roddier et al. advanced the method associated with the DIMM measurement of r_0, which yields the equations for the lateral, longitudinal and total atmospheric coherence length expressed as [43]

$$r_{01} = \left(\frac{2f_L^2\lambda^{5/3}[0.179(\frac{\lambda}{D})^{1/3} - 0.0968(\frac{\lambda}{d})^{1/3}]}{x^2}\right)^{3/5}, \quad (14)$$

$$r_{02} = \left(\frac{2{f_L}^2\lambda^{5/3}[0.179(\frac{\lambda}{D})^{1/3} - 0.0968(\frac{\lambda}{d})^{1/3}]}{y^2}\right)^{3/5}, \quad (15)$$

$$r_0 = \left(\frac{2{f_L}^2\lambda^{5/3}[0.179(\frac{\lambda}{D})^{1/3} - 0.0968(\frac{\lambda}{d})^{1/3}]}{x^2 + y^2}\right)^{3/5}. \quad (16)$$

One is able to measure the variance of the angle of arrival, and then substitute it into the three equations above to obtain the horizontal, vertical and total atmospheric coherence lengths in turn.

It is worth noting that the above two-point-based differential imaging method exists backward. Experimental studies have shown that the measured atmospheric coherence length r_0 at a given time often jumps suddenly by 2–3 cm within a few seconds, and occasionally by nearly 10 cm. The abnormal behavior contradicts the nature of the dynamic disturbance of atmospheric turbulence. It is attributed to the fact that the sample statistics are not sufficient, namely, the wavefront undulation induced by atmospheric turbulence is not identical in each direction, and the differential imaging method only counts the motions of the centroid of two subapertures at a fixed position. Consequently, it requires a long

time to obtain a comprehensive count. However, increasing the number of samples causes a delay in the measurement, while the turbulence has varied. To circumvent this drawback, the authors of [44] designed a multipoint differential imaging method, which increases the number of atmospheric coherence length r_0 samples from the spatial perspective. As such, it enhances the central symmetric statistics based on the concept of spatial groups, and significantly reduces the statistical time required to obtain the atmospheric coherence length r_0, yielding stable and accurate values.

3.2. Wavefront Phase Structure Function Method

The DIMM outlined in Section 3.1 is used to measure r_0 based on the variance of the arrival angle undulation after turbulence, and its accuracy is highly related to the target elevation angle, thus it requires hundreds of frames of data for analysis and calculation. Unlike the DIMM, an instantaneous method for measuring r_0 has been proposed [45–47], which is known as the wavefront structure function method. According to the Kolmogorov theory, assuming that atmospheric turbulence is statistically homogeneous and isotropic as well as temporally ergodic, the phase structure function can be expressed as the time average of the phase difference between two points on the receiving plane, which is

$$D_\Phi(\vec{r_1}, \vec{r_2}) = D_\Phi(r) = \left\langle [\Phi(r) - \Phi(0)]^2 \right\rangle, \tag{17}$$

where $r = |\vec{r_1} - \vec{r_2}|$ denotes the distance between r_1 and r_2, and $\Phi(r)$ is the phase at the distance r from the reference point.

Based on the reconstructed wavefront by the SHWS, the phase structure function is immediately obtained [48]. According to the Kolmogorov model, the phase structure function can be expressed as

$$D_\Phi(r) = \left(\frac{\lambda}{2\pi}\right)^2 6.88\left(\frac{r}{r_0}\right)^{5/3}[1 - 0.975(r/D)^{1/3}] + 2\sigma^2, \tag{18}$$

where D is the diameter of the subaperture of the telescope, and $2\sigma^2$ is the scattering coefficient, which is generally negligible. The schematic sketch of the wavefront phase structure function method is shown in Figure 5. The optical beam originating from the laser propagates through the atmospheric channel. After passing through a concave–convex lens, it is scaled up to a plane wave. Subsequently, another concave–convex lens is applied to scale it down to the receiver side. It is divided into two parts by a beamsplitter. One part is transmitted to the CCD for imaging, and the other is collimated by the lens and incident to the SHWS. The measurement of r_0 using the wavefront structure function method is performed by using five steps.

1. Obtain the Zernike 1 coefficient of the wavefront aberration for a single frame using the SHWS;
2. Subtract the initial Zernike 0 coefficient of the FSO system from the Zernike 1 coefficient of wavefront aberration, noted as Zernike 2;
3. Calculate the corresponding wavefront structure function from Zernike 2, and record it as the measured value;
4. Calculate the corresponding theoretical wavefront structure function according to Equation (17);
5. Find the atmospheric coherence length r_0 by the least-squares estimation based on the measured value of the wavefront structure function from step (3) and the theoretical value of the wavefront structure function from step (4).

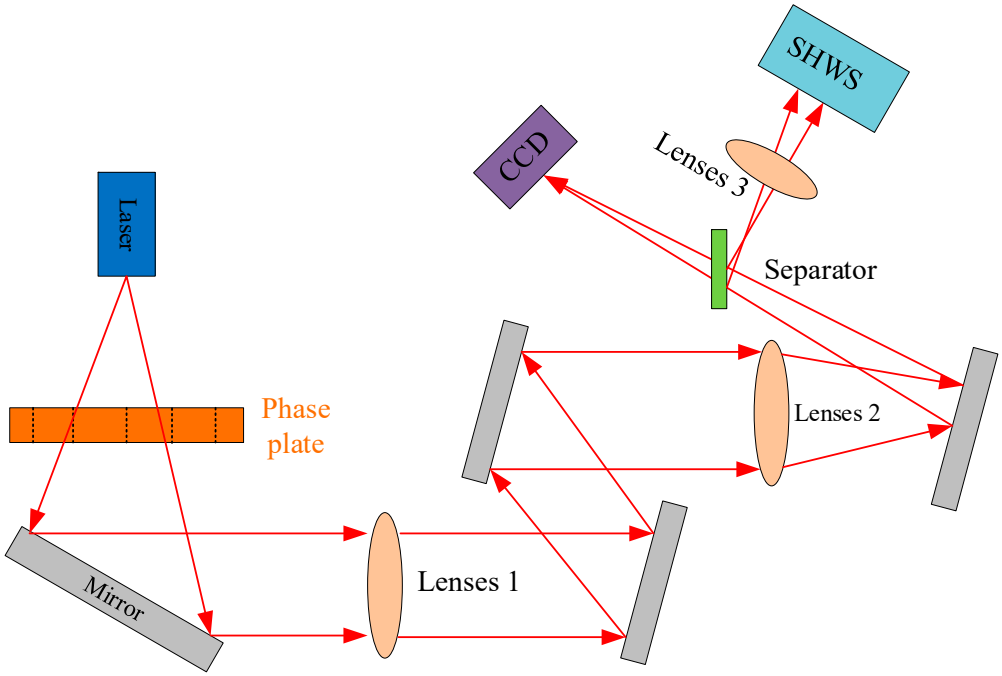

Figure 5. Schematic sketch of the wavefront phase structure function method.

3.3. Slope Difference Method

In contrast to the two-observation-point approach in the DIMM, the slope difference method uses an array of slopes measured from the SHWS to capture the turbulence effects in statistics [49–53]. Since the spatial–temporal slope structure implicates both spatial and temporal fluctuations resulting from the atmospheric turbulence, the structure function is useful for characterizing both statistics. The spatial–temporal slope structure function is defined as the mean squared difference between the slopes measured in any two subapertures. One advantage of the slope structure function is that it is insensitive to system jitter and overall wavefront tilt. The inherent mathematical processing associated with the slope structure function offsets any overall tilt that the subapertures bring. On the other side, the insensitivity to system jitter effectively avoids the systemic errors when measurements are operated with a moving or vibrating platform.

The SHWS splits the pupil of the imaging system into a limited number of sub-optical paths. Each sensor element focuses incident light onto the CCD with a subaperture lens. As such, an array of points in the focal plane is created. We assume that the subapertures are squares with the same orientation, but in an arbitrary geometric arrangement. The centroid position of the irradiance points on the detector array is calculated according to occupied pixels in the CCD. The centroid position is related to the average slope or gradient of the wavefront on the subaperture lens. The average slope gradient is written as [49],

$$\eta_\chi(x,t) = \int dr[\nabla Z(r-x)\chi]\theta(r,t), \tag{19}$$

where $\eta_\chi(x,t)$ is the measured slope in direction χ centered at x and time t; the wavefront phase is specified as $\theta(r, t)$; and ∇ is the gradient operator. χ is a unit vector in the direction of slope measurement sensitivity. The function $Z(r)$ is the aperture function with

$$Z(r) = \begin{cases} 1, r \in R \\ 0, else \end{cases}, \tag{20}$$

where R is the aperture diameter. Combining the definition of the structure function and the slope measurements given in Equation (18), the slope structure function can be expressed as

$$\begin{aligned} D_{\eta}^{\chi}(x,x',t,t') &= \left\langle [\eta_{\chi}(x,t) - \eta_{\chi}(x',t')]^2 \right\rangle \\ &= \left\langle [\int dr[\nabla Z(r-x)\chi]\theta(r,t) - \int dr[\nabla Z(r-x')\chi]\theta(r,t')]^2 \right\rangle, \end{aligned} \tag{21}$$

where $D_{\eta}^{\chi}(x,x',t,t')$ is the slope structure function of the subaperture slope measurement centered at x and at moment t and the phase structure function can be expressed as

$$D_{\varphi}(x,x',t,t') = \left\langle [\theta(x,t) - \theta(x',t')]^2 \right\rangle. \tag{22}$$

Based on the basic variations of the slope structure function, the phase structure function, and the atmospheric coherence length variable, the spatial slope structure function can be expressed by a dimensionless integral as [49]

$$\begin{aligned} D_{\eta}^{\chi}(\Delta x_s, \Delta y_s, \Delta x_t, \Delta y_t) \quad &= \Upsilon_{\beta} d^{-2} (\tfrac{d}{r_0})^{\beta-2} \int du \int_0^{\infty} dv W(z) tui(u) \\ &\times \{ [2|\Delta x_s + \Delta x_t(z) - 1, u + \Delta x_s + \Delta x_s(z)|^{\beta-2} \\ &- |\Delta x_s + \Delta x_t(z) + 1, u + \Delta y_s + \Delta y_t(z)|^{\beta-2} \\ &- 2(|0,u|_{\beta-2} - |1,u|_{\beta-2}) \}, \end{aligned} \tag{23}$$

where Δx_s, Δy_s, $\Delta x_t(z)$ and $\Delta y_t(z)$ represents normalized spatial and temporal separation of subaperture slope measurements; $x_s = (x - x')/d$, $\Delta y_s = (y - y')/d$, $\Delta x_t(z) = W_x(z)(t - t')/d$, $\Delta y_t(z) = W_x(z)(t - t')/d$; $tri(u)$ is a triangular function; β is the power law of the power spectrum of the refractive index fluctuations and γ_{β} is function of the power law. $W(z)$ is a normalized profile. It is clear from the above equations that the slope structure function depends on these normalized separations as well as on the atmospheric parameters, γ_{β}, r_0 and $W(z)$.

The slope structure function is calculated based on the average slope measured by the SHWS, which is used to evaluate r_0. It has been shown that the direct use of slope measurements to characterize atmospheric turbulence is feasible and less computationally intensive than wavefront phase reconstruction.

3.4. Wavefront Phase Variance Method

The wavefront phase variance method uses the SHWS to measure the variance of the wavefront phase induced by atmospheric turbulence, which is used to obtain r_0 [17,54]. Compared to the wavefront structure function method, it has less exposure time, thus the measurement would be more accurate. Additionally, its operation is tractable.

According to Equation (17), the phase structure function can be expressed as the time average of the phase difference between two points. To observe the wavefront aberration caused by atmospheric turbulence, a plane wave is introduced as a reference. The instantaneous wavefront phase variance over the aperture can be expressed as

$$\begin{aligned} \sigma^2(R,t) \quad &= \tfrac{1}{\pi R^2} \int_{\psi=0}^{\psi=2\pi} \int_{r=0}^{r=R} [(\Phi(r,\psi,t) - \Phi(0,0,t)]^2 r dr d\psi \\ &= \tfrac{1}{\pi R^2} \int_{\psi=0}^{\psi=2\pi} \int_{r=0}^{r=R} D_{\Phi}(r) r dr d\psi, \end{aligned} \tag{24}$$

where R is the aperture radius, and the horizontal line indicates the statistical average in time. The relationship between the wavefront error variance and the phase structure function can be obtained by averaging the left and right sides of the above equation in

time. According to the Kolmogorov model, the structure function of a plane wave can be expressed as

$$D_\Phi(r) = 6.88\left(\frac{r}{r_0}\right)^{5/3}. \tag{25}$$

If the atmospheric turbulence is assumed to be statistically homogeneous and isotropic, then the wavefront error variance averaged over time is equal to the phase structure function averaged over space. Now Equation (24) becomes

$$\overline{\sigma^2(R,t)} \approx \frac{1}{\pi R^2} \int_{\psi=0}^{\psi=2\pi} \int_{r=0}^{r=R} 6.88(r/r_0)^{5/3} r dr d\psi = 3.75(R/r_0)^{5/3}. \tag{26}$$

It follows that the value of the atmospheric coherence length can be estimated as

$$r_0 = \left(\frac{3.75 \times R^{5/3}}{\overline{\sigma^2(R,t)}}\right)^{3/5}. \tag{27}$$

The principle of the wavefront phase variance method is demonstrated in Figure 6.

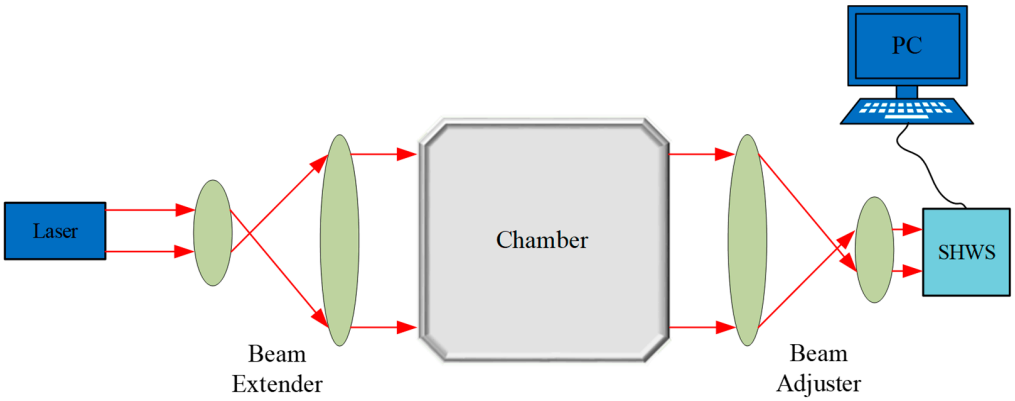

Figure 6. Schematic sketch of wavefront phase variance method.

The laser launches the optical beam, which is scaled up by a beam expander. Subsequently, the beam travels through an atmospheric chamber mimicking turbulence. On the receiving side, the beam is scaled down to match the aperture size of the SHWS.

Since the aperture size of the Shack–Hartman sensor is generally smaller than the internal scale l_0 of the turbulent cells, when the aperture radius is small, r_0 is not a constant. The Kolmogorov model is appropriate within the inertial subrange only. The inner scale l_0 is usually between a few millimeters and a few centimeters, decreasing with the turbulence strength. The outer scale L_0 is usually in the order of meters. Thus, the Kolmogorov model is inappropriate for the analysis of the FSO link with an optical beam diameter less than l_0. That is, the methodology associated with the wavefront phase variance above may fail. In this regard, the optical beam width needs to be extended so that enough turbulence information can be sampled. The beam is scaled down by a beam adjuster after propagating over the atmospheric channel to match the aperture of the SHWS. By doing so, the effective aperture of the sensor is expanded. According to Equation (27), the atmospheric coherence length r_0 is evaluated by the use of the measured phase variance and R. It is worth noting that the method depends strongly on the effective aperture of the sensor used in the experimental setup. When the aperture size of the SHWS is close to the inner scale l_0, the model that incorporates the inner scale factor, instead of the Kolmogorov model, could be adopted.

4. Discussion

The atmospheric coherence length reflects the optical wavefront distortion caused by atmospheric turbulence, which is able to predict the performance of FSO links operating under conditions of atmospheric turbulence. In this paper, the measurement methods associated with the atmospheric coherence length for the FSO links were reviewed. These include the temperature structure measurement method, the scintillation method, the radar measurement method, the differential imaging method, the wavefront structure function method, the slope difference method and the wavefront phase variance method.

The temperature structure measurement method, laser scintillation method and radar measurement method calculate the atmospheric refractive index structure parameter by measuring the temperature, scintillation index and scattering cross section, and then retrieve the atmospheric coherence length. However, the temperature structure measurement method fails to measure in high altitude. The scintillometer is appropriate for the measurement in a limited range only due to the scintillation saturation effect. The radar measurement method is only suitable for the measurement of fixed-point targets. Furthermore, it is cumbersome to deploy and the cost is huge. The measurement of r_0 based on the SHWS has drawbacks. The non-orthogonality of the polynomial derivatives introduces modal cross-coupling, which affects the variance. The wavefront phase variance method, which has a short exposure time and a large enough sample, can increase the accuracy of the calculation. It also has some improvements to address the limitation of the aperture size of the wavefront sensor.

As for the measurements resulting from the methods described above, differences may exist due to intrinsic defects in the employed specific instruments. The temperature structure measurement method is highly reliant on the design of the Wheatstone bridge. The authors of [25] demonstrated that the scintillometer may provide larger turbulence strength than the DIMM. This might be attributed to the APD shot noise in the scintillometer receiver, which may be coupled with a measurement path. The radar measurement method depends on the calibration accuracy [35,36]. Noise, aliasing and modal cross-coupling are deleterious effects introduced by the SHWS, which degrade the quality of the wavefront reconstruction and limit the accuracy of the wavefront structure function method, the slope difference method and the wavefront phase variance method [45].

Author Contributions: Conceptualization, M.L. and P.Z.; writing—original draft preparation, P.Z.; writing—review and editing, M.L. and J.H.; supervision, M.L.; project administration, M.L.; funding acquisition, M.L. and J.H. All authors have read and agreed to the published version of the manuscript.

Funding: This research was funded by the National Natural Science Foundation of China (Grant 61805176, Grant 62001327).

Institutional Review Board Statement: Not applicable.

Informed Consent Statement: Not applicable.

Data Availability Statement: Not applicable.

Conflicts of Interest: The authors declare no conflict of interest.

References

1. Scarani, V.; Bechmann-Pasquinucci, H.; Cerf, N.J.; Dušek, M.; Lütkenhaus, N.; Peev, M. The security of practical quantum key distribution. *Rev. Mod. Phys.* **2009**, *81*, 1301–1350. [CrossRef]
2. Li, M.; Wang, T.; Han, J.; Yu, Z.; Cvijetic, M.; Ye, H.; Liu, Y. Free space continuous-variable quantum key distribution with practical links. *J. Opt. Soc. Am. B* **2020**, *37*, 3690–3697. [CrossRef]
3. Chowdhury, M.Z.; Shahjalal, M.; Hasan, M.; Jang, Y.M. The role of optical wireless communication technologies in 5G/6G and IoT solutions: Prospects, directions, and challenges. *Appl. Sci.* **2019**, *9*, 4367. [CrossRef]
4. Chan, V.W.S. Free-space optical communications. *J. Lightwave Technol.* **2006**, *24*, 4750–4762. [CrossRef]
5. Trichili, A.; Cox, M.A.; Ooi, B.S.; Alouini, M.-S. Roadmap to free space optics. *J. Opt. Soc. Am. B* **2020**, *37*, A184–A201. [CrossRef]
6. Khalighi, M.A.; Uysal, M. Survey on Free Space Optical Communication: A Communication Theory Perspective. *IEEE Commun. Surv. Tutor.* **2014**, *16*, 2231–2258. [CrossRef]

7. Li, M.; Cvijetic, M. Coherent free space optics communications over the maritime atmosphere with use of adaptive optics for beam wavefront correction. *Appl. Opt.* **2015**, *54*, 1453–1462. [CrossRef]
8. Li, M.; Gao, W.; Cvijetic, M. Slant-path coherent free space optical communications over the maritime and terrestrial atmospheres with the use of adaptive optics for beam wavefront correction. *Appl. Opt.* **2017**, *56*, 284–297. [CrossRef]
9. Li, X.; Geng, T.; Gu, Y.; Tian, R.; Gao, S. Compensation for In-Phase/Quadrature Phase Mismatch in Coherent Free-Space Optical QPSK Communication Systems. *Appl. Sci.* **2021**, *11*, 2543. [CrossRef]
10. Rachmani, R.; Zilberman, A.; Arnon, S. Computer Backplane with Free Space Optical Links: Air Turbulence Effects. *J. Lightwave Technol.* **2012**, *30*, 156–162. [CrossRef]
11. Xiaoming, Z.; Kahn, J.M. Free-space optical communication through atmospheric turbulence channels. *IEEE Trans. Commun.* **2002**, *50*, 1293–1300. [CrossRef]
12. Andrews, L.C.; Phillips, R.L. *Laser Beam Propagation through Random Media*, 2nd ed.; SPIE Press: Bellingham, WA, USA, 2005.
13. Schmidt, J.D. *Numerical Simulation of Optical Wave Propagation with Examples in MATLAB*; SPIE Press: Bellingham, WA, USA, 2010.
14. Andrews, L.C.; Phillips, R.L.; Hopen, C.Y. *Laser Beam Scintillation with Applications*; SPIE Press: Bellingham, WA, USA, 2001.
15. Brown, D.M.; Juarez, J.C.; Brown, A.M. Laser differential image-motion monitor for characterization of turbulence during free-space optical communication tests. *Appl. Opt.* **2013**, *52*, 8402–8410. [CrossRef]
16. Zheng, D.; Li, Y.; Zhou, H.; Bian, Y.; Yang, C.; Li, W.; Qiu, J.; Guo, H.; Hong, X.; Zuo, Y.; et al. Performance enhancement of free-space optical communications under atmospheric turbulence using modes diversity coherent receipt. *Opt. Express* **2018**, *26*, 28879–28890. [CrossRef]
17. Gao, W.; Cvijetic, M. Evaluation of Air Turbulence Impact Based on Wavefront Reconstruction. In Proceedings of the Conference on Lasers and Electro-Optics, San Jose, CA, USA, 14 May 2017; Optical Society of America: San Jose, CA, USA, 2017; p. AM4B.3.
18. Webb, A.J.; Roggemann, M.C.; Whiteley, M.R. Atmospheric turbulence characterization through multiframe blind deconvolution. *Appl. Opt.* **2021**, *60*, 5031–5036. [CrossRef]
19. Charnotskii, M. Passive scintillometer: Theory and field measurements. *J. Opt. Soc. Am. A* **2021**, *38*, 1766–1776. [CrossRef]
20. Killinger, D.; Menyuk, N. Effect of turbulence-induced correlation on laser remote sensing errors. *Appl. Phys. Lett.* **1981**, *38*, 968–970. [CrossRef]
21. Measures, R.M. *Laser Remote Sensing: Fundamentals and Applications*; Wiley-Interscience: New York, NY, USA, 1984.
22. Fried, D.L. Optical Resolution Through a Randomly Inhomogeneous Medium for Very Long and Very Short Exposures. *J. Opt. Soc. Am.* **1966**, *56*, 1372–1379. [CrossRef]
23. Wang, T.-I.; Ochs, G.; Clifford, S. A saturation-resistant optical scintillometer to measure Cn2. *JOSA* **1978**, *68*, 334–338. [CrossRef]
24. Tunick, A. Statistical analysis of measured free-space laser signal intensity over a 2.33 km optical path. *Opt. Express* **2007**, *15*, 14115–14122. [CrossRef]
25. Brown, D.M.; Hanna, R.T.; Brown, A.M.; Hixson, J.G.; Baldwin, K.C. Numerical simulation of a large area scintillometer and laser differential image motion monitor. *Appl. Opt.* **2022**, *61*, 10–21. [CrossRef] [PubMed]
26. Frehlich, R.G.; Ochs, G.R. Effects of saturation on the optical scintillometer. *Appl. Opt.* **1990**, *29*, 548–553. [CrossRef]
27. Hill, R.J.; Ochs, G.R. Inner-scale dependence of scintillation variances measured in weak scintillation. *JOSA A* **1992**, *9*, 1406–1411. [CrossRef]
28. Ochs, G.; Cartwright, W. An Optical Device for Path-Averaged Measurements of Cn2. In Proceedings of the SPIE 0277, Atmospheric Transmission, Washington, DC, USA, 28 July 1981.
29. User's Guide. *LOA-005 Long Baseline Optical Anemomete/Turbulence Sensors*; Optical Scientific, Inc.: Gaithersburg, MD, USA, 2022; Available online: http://www.opticalscientific.com/ (accessed on 18 November 2021).
30. Vorontsov, A.M.; Vorontsov, M.A.; Filimonov, G.A.; Polnau, E. Atmospheric Turbulence Study with Deep Machine Learning of Intensity Scintillation Patterns. *Appl. Sci.* **2020**, *10*, 8136. [CrossRef]
31. Kohsiek, W.; Meijninger, W.M.L.; Debruin, H.A.R.; Beyrich, F. Saturation of the Large Aperture Scintillometer. *Bound. Layer Meteorol.* **2006**, *121*, 111–126. [CrossRef]
32. Hill, R.J. Saturation resistance and inner-scale resistance of a large-aperture scintillometer: A case study. *Appl. Opt.* **1981**, *20*, 3822–3824. [CrossRef] [PubMed]
33. Beyrich, F.; Hartogensis, O.K.; de Bruin, H.A.; Ward, H.C. Scintillometers. In *Springer Handbook of Atmospheric Measurements*; Springer: Berlin/Heidelberg, Germany, 2021; pp. 969–997.
34. Tatarski, V.I. *Wave Propagation in a Turbulent Medium*; Courier Dover Publications: New York, NY, USA, 2016.
35. Wainwright, C.E.; Bonin, T.A.; Chilson, P.B.; Gibbs, J.A.; Fedorovich, E.; Palmer, R.D. Methods for evaluating the temperature structure-function parameter using unmanned aerial systems and large-eddy simulation. *Bound. Layer Meteorol.* **2015**, *155*, 189–208. [CrossRef]
36. Scipión, D.E.; Lawrence, D.A.; Milla, M.A.; Woodman, R.F.; Lume, D.A.; Balsley, B.B. Simultaneous observations of structure function parameter of refractive index using a high-resolution radar and the DataHawk small airborne measurement system. *Ann. Geophys.* **2016**, *34*, 767–780. [CrossRef]
37. Hocking, W.; Mu, P. Upper and middle tropospheric kinetic energy dissipation rates from measurements of Cn2—Review of theories, in-situ investigations, and experimental studies using the Buckland Park atmospheric radar in Australia. *J. Atmos. Sol. Terr. Phys.* **1997**, *59*, 1779–1803. [CrossRef]

38. Cohn, S.A. Radar measurements of turbulent eddy dissipation rate in the troposphere: A comparison of techniques. *J. Atmos. Ocean. Technol.* **1995**, *12*, 85–95. [CrossRef]
39. User's Guide. *DELTA Imaging Path Turbulence Monitor, PM-02-600*; MZA Inc.: Westlake Village, CA, USA, 2022. Available online: https://www.mza.com/doc/misc/MZA_DELTA_PM-02-600_Specifications.pdf (accessed on 20 November 2021).
40. Zuraski, S.M. Profiling Atmospheric Turbulence Using a Dynamically Ranged Rayleigh Beacon System. Ph.D. Thesis, Air Force Institute of Technology, Dayton, OH, USA, 2021.
41. Berdja, A. On the DIMM interpretation of non-Kolmogorov turbulence in the atmospheric surface layer. *Mon. Not. R. Astron. Soc.* **2010**, *409*, 722–726. [CrossRef]
42. Bose-Pillai, S.R.; McCrae, J.E.; Rucci, M.A.; Kwasniewski, E.M.; Fiorino, S.T. Estimation of Fried's Coherence Diameter from Differential Motion of Features in Time-lapse Imagery. In Proceedings of the 2019 IEEE Aerospace Conference, Big Sky, MT, USA, 2–9 March 2019.
43. Sarazin, M.; Roddier, F. The ESO differential image motion monitor. *Astron. Astrophys.* **1990**, *227*, 294–300.
44. Aristidi, E.; Fanteï-Caujolle, Y.; Ziad, A.; Dimur, C.; Chabé, J.; Roland, B. A new generalized differential image motion monitor. In Proceedings of the SPIE 9145, Ground-based and Airborne Telescopes V, 91453G, Montréal, QC, Canada, 22 July 2014.
45. Andrade, P.P.; Garcia, P.J.; Correia, C.M.; Kolb, J.; Carvalho, M.I. Estimation of atmospheric turbulence parameters from Shack–Hartmann wavefront sensor measurements. *Mon. Not. R. Astron. Soc.* **2019**, *483*, 1192–1201. [CrossRef]
46. Rao, C.; Jiang, W.; Ling, N. Atmospheric characterization with Shack-Hartmann wave-front sensor for non-Kolmogorov turbulence. *Opt. Eng.* **2002**, *41*, 534–541. [CrossRef]
47. Sauvage, C.; Robert, C.; Mugnier, L.M.; Conan, J.M.; Cohard, J.M.; Nguyen, K.L.; Irvine, M.; Lagouarde, J.P. Near ground horizontal high resolution Cn2 profiling from Shack–Hartmann slopeand scintillation data. *Appl. Opt.* **2021**, *60*, 10499–10519. [CrossRef] [PubMed]
48. Dayton, D.; Pierson, B.; Spielbusch, B.; Gonglewski, J. Atmospheric structure function measurements with a Shack–Hartmann wave-front sensor. *Opt. Lett.* **1992**, *17*, 1737–1739. [CrossRef] [PubMed]
49. Silbaugh, E.E.; Welsh, B.M.; Roggemann, M.C. Characterization of atmospheric turbulence phase statistics using wave-front slope measurements. *J. Opt. Soc. Am. A* **1996**, *13*, 2453–2460. [CrossRef]
50. Jiang, Z.; Dai, Y.; Li, F.; Cheng, X.; Gong, S. Numerical simulation of Shack–Hartmann wavefront sensor to characterize the turbulence phase statistics. *Opt. Lasers Eng.* **2006**, *44*, 466–478. [CrossRef]
51. Butterley, T.; Wilson, R.W.; Sarazin, M. Determination of the profile of atmospheric optical turbulence strength from SLODAR data. *Mon. Not. R. Astron. Soc.* **2006**, *369*, 835–845. [CrossRef]
52. Védrenne, N.; Michau, V.; Robert, C.; Conan, J.-M. Cn2 profile measurement from Shack-Hartmann data. *Opt. Lett.* **2007**, *32*, 2659–2661. [CrossRef]
53. Laidlaw, D.J.; Reeves, A.P.; Singhal, H.; Calvo, R.M. Characterizing turbulence profile layers through celestial single-source observations. *Appl. Opt.* **2022**, *61*, 498–504. [CrossRef]
54. Zuraski, S.; Beecher, E.; McCrae, J.; Fiorino, S. Turbulence profiling using pupil plane wavefront data derived Fried parameter values for a dynamically ranged Rayleigh beacon. *Opt. Eng.* **2020**, *59*, 081807. [CrossRef]